Research Article Vol. 12, No. 7 / 1 Jul 2022 / Optical Materials Express 2679
Optical Materials EXPRESS

Spike propagation in a nanolaser-based optoelectronic neuron

IGNACIO ORTEGA-PIWONKA,[1,2,*] MATĚJ HEJDA,[3] JUAN ALANIS,[3] JOÃO LOURENÇO,[4] ANTONIO HURTADO,[3] JOSÉ FIGUEIREDO,[4] BRUNO ROMEIRA,[5] AND JULIEN JAVALOYES[1,2]

[1]*Institute of Applied Computing and Community Code (IAC-3), University of the Balearic Islands, Carretera de Valldemossa, km. 7.5, Palma, Postcode 07122, Spain*
[2]*Department of Physics, University of the Balearic Islands, Carretera de Valldemossa, km. 7.5, Palma, Postcode 07122, Spain*
[3]*Institute of Photonics, University of Strathclyde, 16 Richmond St, Glasgow G1 1XQ, United Kingdom*
[4]*Centra-Ciências and Departamento de Física, Faculdade de Ciências, Universidade de Lisboa, 1749-016 Lisboa, Portugal*
[5]*Ultrafast Bio- and Nanophotonics, INL - International Iberian Nanotechnology Laboratory, Av. Mestre José Veiga s/n, 4715-330 Braga, Portugal*
[*]*ignacio.ortega.piwonka@gmail.com*

Abstract: With the recent development of artificial intelligence and deep neural networks, alternatives to the Von Neumann architecture are in demand to run these algorithms efficiently in terms of speed, power and component size. In this theoretical study, a neuromorphic, optoelectronic nanopillar metal-cavity consisting of a resonant tunneling diode (RTD) and a nanolaser diode (LD) is demonstrated as an excitable pulse generator. With the proper configuration, the RTD behaves as an excitable system while the LD translates its electronic output into optical pulses, which can be interpreted as bits of information. The optical pulses are characterized in terms of their width, amplitude, response delay, distortion and jitter times. Finally, two RTD-LD units are integrated via a photodetector and their feasibility to generate and propagate optical pulses is demonstrated. Given its low energy consumption per pulse and high spiking rate, this device has potential applications as building blocks in neuromorphic processors and spiking neural networks.

1. Introduction

With the ever-increasing amount of data involved in problems addressed by industry and academia, algorithms based on machine learning and neural networks are gaining more and more relevance, with the subsequent demand for qualified professionals and pertinent hardware. Current computers based on the Von Neumann architecture [1] are not meeting the expectations to execute such complex algorithms efficiently in terms of time and energy consumption. The causes behind this lack of efficiency are multiple and include the discrete nature of the variables treated by processors on the fundamental level (i.e., digital coding), dissipation in electrical interconnections, inability by processors to treat data and algorithms differently, data transfer between physically distant units and component size limitations set by quantum effects.

Consequently, a new computational architecture is required, where the fundamental blocks in the processors – the neurons of the brain, so to speak – are able to process variables in a more continuous manner than binary coding. The idea is to have each block emulate the role of a single node (e.g., a neuron) in a multilayer deep neural network, in contrast to conventional processors, where multiple transistors are required to reproduce a single node. In this regard, blocks that emulate the behavior of actual, biological neurons, able to process and transmit information in

#451706 https://doi.org/10.1364/OME.451706
Journal © 2022 Received 24 Dec 2021; revised 4 Mar 2022; accepted 17 Mar 2022; published 22 Jun 2022

Optical Materials EXPRESS

the form of spikes at arbitrary times, are becoming a promising alternative. Spiking signaling has the advantage of being robust in the presence of noise, just like binary signaling, but it also involves lower energy consumption, as energy is spent only at the very specific and short moment of time when a spike is triggered. Examples of neuromorphic processors developed so far include the IBM True-North [2], the Intel Loihi 2 [3], the BRAIN Initiative [4] and the Innatera chip [5].

The architectures mentioned above are electrical implementations. They operate at frequencies in the order of the kHz and energy consumption in the order of pJ per spike. This performance can be further improved by propagating information as optical pulses rather than electrical ones, as electrical interconnection dissipation is avoided and electromagnetic interference is reduced [6]. So far, photonic spiking neurons have been implemented using graphene excitable lasers [7], time-delayed optoelectronic resonators [8], phase change materials [9] and vertical-cavity surface-emitting lasers (VCSELs) [10–12]. These neurons have nevertheless relatively large micrometric size footprints. New approaches have been proposed in order to miniaturize light-emitting devices using photonic crystal cavities [13–15], metallic cavities [16] and plasmonic cavities [17].

The necessity to overcome the diffraction limitation of light and the challenges of achieving lasing in nanocavities are addressed in a study by Romeira et al. [18]. Here, a nanoscale, optoelectronic artificial spiking neuron is proposed and its performance analyzed. It consists of a double barrier quantum well resonant tunneling diode (DBQW-RTD, or RTD for short) monolithically integrated with a sub-λ, metal cavity, double hetero-structure nanoLED. The RTD is an electrical device with a non-ohmic current-voltage characteristic that exhibits a region of negative differential conductance (NDC) embedded between two regions of positive differential conductance (PDC). When biased in the proximity to the NDC region and perturbed with square voltage pulses, the RTD responds with an electrical spike, as long as said pulse has a sufficiently high amplitude, over a certain threshold. Responses to sub-threshold pulses on the other hand are negligible. Thus, the RTD behaves as an *excitable* system, much like biological neurons [19]. The electrical current spikes drive the nanoLED, modulating the light intensity output in the form of optical spikes. This artificial, hybrid neuron is demonstrated as a promising candidate to integrate a prospective neuromorphic processor, given its low activation voltage (under 10 mV), fast spiking rate (> 1 GHz) and reduced size (~0.01 μm^2).

The key difference between the nanolaser optoelectronic neuron and all-optical neurons is that the neuron signal in an all-optical neuron typically represents changes in the material nonlinear properties which are generally weak and power inefficient leading to challenges of all-optical neurons to drive other neurons without substantial optical amplification. In our case, the output of the neuron can be appreciably stronger than the input (taking advantage of the NDC amplification factor), which is not generally the case for all-optical neurons. An alternative to this is to use active laser sources with stronger material nonlinearities [20–22].

In this work we present a nanophotonic spiking neuron where a low Q-cavity, nanolaser diode (nanoLD, or LD for short) is chosen as the optical component. NanoLEDs have limited power output (< 1 μW) and speed (~1 GHz), since it is challenging to achieve spontaneous emission enhancement (Purcell effect) in practical nanoLEDs operating at room-temperature [23]. Nanolasers may enable direct modulation rates larger than 40 Gb/s at power levels adequate for short-distance and low-energy optical interconnects [23]. A description on the dynamics of the electrical and optical components is presented separately. Then, the integrated node is demonstrated as an excitable optical pulse generator, for which different configurations are found, including long and short-lived light pulses and regimes where the nanoLD is permanently emitting and bits of information are sent by momentarily increasing, decreasing or deactivating the emission. These pulses are quantitatively characterized by applying eye diagram techniques [24,25]. Special attention is paid to the fluctuating character of the responses, considering the

Optical Materials EXPRESS

stochastic nature of the model. Finally, pulse propagation between two optoelectronic nodes connected via a photodetector is demonstrated.

The paper is structured as follows. In section 2, the theoretical model that accounts for the dynamics of the optoelectronic neuron is presented, including equations, variables and parameters. In section 3, the electrical part of the neuron, namely, an RTD connected to an external source of voltage, is briefly discussed and the configuration to behave as an excitable electrical spike generator is demonstrated. In section 4, the optical part –a nanoLD connected to an external current–, is studied. A current threshold is identified, only beyond which the nanoLD emits light. In section 5, The integrated RTD-LD node subjected to square voltage pulses is considered, configurations suitable for optical pulse emission are identified and the optical pulses are quantitatively characterized. In section 6, pulse propagation along two integrated RTD-LD nodes is demonstrated. The conclusion are discussed in section 7.

2. Theoretical model

The proposed optoelectronic artificial neuron is made of a nanoscopic resonant tunneling diode (nanoRTD or RTD) monolithically integrated with a low-Q cavity nanolaser diode (nanoLD or LD) in a nanopillar metal-cavity, as shown in Fig. 1(a). A simplified scheme of the device is depicted in Fig. 1(b). The case of an RTD using InP lattice matched materials is assumed [26]. On the other hand, the nanolaser is assumed as a semiconductor pillar (e.g. InP/InGaAs/InP) surrounded by an isolating dielectric material and then encapsulated with metal [23]. These materials are lattice-matched with the materials assumed for the RTD device case. Therefore, a monolithic integrated nanolaser RTD can be envisioned. We note however, the model presented here is quite general and could be applied to other laser cavities, such as photonic crystal or plasmonic cavities and other quantum dot/well/bulk gain materials.

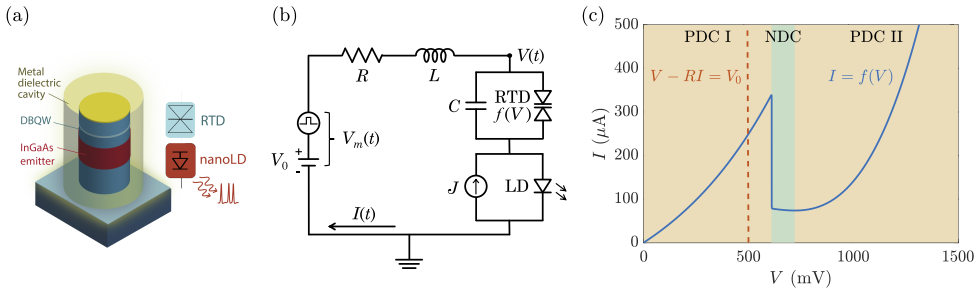

Fig. 1. a) Nanopillar metal-cavity integrating the optoelectronic RTD-LD spiking neuron. b) Schematics of the equivalent circuit. c) Nonlinear current-voltage characteristic of the nanoRTD (solid blue curve), load line when the circuit is biased at a constant input voltage $V_m(t) = V_0 = 500\,\text{mV}$ (dashed orange line), PDC regions (yellow areas) and NDC region (green area).

The dynamics of the optoelectronic RTD-LD circuit is modeled by a system of four differential equations and four variables,

$$C\frac{dV}{dt} = I - f(V), \tag{1}$$

$$L\frac{dI}{dt} = V_m(t) - V - RI. \tag{2}$$

$$\frac{dE}{dt} = \frac{1-i\alpha}{2}\left(\gamma_m(N-N_0) - \frac{1}{\tau_p}\right)E + \sqrt{\tfrac{1}{2}\gamma_m N}\left(\xi_x(t) + i\xi_y(t)\right), \tag{3}$$

$$\frac{dN}{dt} = \frac{J+I}{q_e} - (\gamma_l + \gamma_m + \gamma_{nr})N - \gamma_m(N-N_0)|E|^2. \tag{4}$$

Optical Materials EXPRESS

Equations (1), (2) account for the electrical part of the circuit (i.e., nanoRTD) while Eqs. (3), (4) account for the optical part (i.e., nanoLD). Equations (1), (2) are derived from the laws of Kirchhoff. Here, $V(t)$ is the voltage along the nanoRTD and $I(t)$ is the circuit's total current. R and L are the intrinsic resistance and inductance of the circuit while C is the capacitance of the nanoRTD. Given the dimensions of the system under study, realistic choices for these parameters are $R = 10\,\Omega$, $L = 126\,\text{nH}$ and $C = 2\,\text{fF}$. $V_m(t)$ is an external input voltage used to drive the nanoRTD. The function $f(V)$ accounts for the nonlinear current-voltage (I-V) characteristic of the nanoRTD. The double barrier quantum well (DBQW) nanostructure inside the nanoRTD allows for quantum resonance between the Fermi energy of incident electrons and the barrier confinement energy levels. As a result, the probability for an incident electron to cross the barrier and thus the mean current across the RTD are locally maximized for certain voltages. Consequently, the I-V characteristic exhibits one or more finite regions of negative differential conductance [27,28]. In this study we assume the case of a DBQW with AlAs barriers and an InGaAs quantum well. An analytical expression $I = f(V)$ is used to fit the static I-V characteristic [29],

$$f(V) = a \ln\left(\frac{1 + e^{\frac{q_e}{k_B T}(b-c+n_1 V)}}{1 + e^{\frac{q_e}{k_B T}(b-c-n_1 V)}}\right) \times \left(\frac{\pi}{2} + \tan^{-1}\left(\frac{c - n_1 V}{d}\right)\right) + h\left(e^{\frac{q_e}{k_B T} n_2 V} - 1\right). \tag{5}$$

Here, T is the temperature, q_e is the electron charge and k_B is the Boltzmann's constant. The parameters a, b, c, d, n_1, n_2, h depend on the geometry of the barrier and the confinement energy levels. The device studied here operates at room temperature (300°C) and the following parameter values are found after fitting experimental data: $a = -5.5 \times 10^{-5}\,\text{A}$, $b = 0.033\,\text{V}$, $c = 0.113\,\text{V}$, $d = -2.8 \times 10^{-6}\,\text{V}$, $n_1 = 0.185$, $n_2 = 0.045$, $h = 18 \times 10^{-5}\,\text{A}$. Figure 1(c) illustrates the nonlinear current-voltage characteristic resulting from Eq. (5) with the parameter values mentioned above. It exhibits a single region of negative differential conductance embedded in between two regions of positive differential conductance, labeled as NDC, PDC I and PDC II, respectively. The curve peak is located at $V = 609.6$ mV. At the right of the peak, the current abruptly drops from 340 μA to 80 μA in a span of less than 1 mV. Further rightwards, $f(V)$ continues to decrease although with a much more moderate rate, until it reaches a local minimum at $V = 720.7$ mV. Beyond this valley, $f(V)$ increases again at a fairly exponential rate.

Equations (3), (4) are derived from the standard rate model that describes the dynamics for the photon number and carrier population in a laser diode [23,30–33]. N is the carrier number and E is a complex field such that the photon number is given by $S = |E|^2$. This model has been simplified by taking a linear gain $G = \gamma_m(N - N_0)$ and multiplicative noise (defined via uncorrelated white noise functions $\xi_x(t)$ and $\xi_y(t)$) that produce fluctuations in the semiconductor bandgap. $\alpha = 2$ is a factor that accounts for the polarization of the complex field E; its choice is rather arbitrary. $N_0 = 5 \times 10^5$ is the transparency carrier number. $\tau_p = 5 \times 10^{-13}$ s is the photon lifetime. These values typically correspond to the the case of low-Q metal cavity nanolasers. $\gamma_m = 10^7\,\text{s}^{-1}$ and $\gamma_l = 10^9\,\text{s}^{-1}$ are respectively the spontaneous emission rate into the lasing mode, and the radiative decay into the leaky modes. These coefficients have been chosen to ensure a spontaneous emission factor of $\beta = \gamma_m/(\gamma_m + \gamma_l) = 0.0099$, proper of nanoscale lasers. $\gamma_{nr} = 2 \times 10^9\,\text{s}^{-1}$ is the non-radiative spontaneous emission coefficient, which also can have a strong role in the performance around threshold operation. q_e is the electron charge. J is an input bias current used to drive the nanoLD.

In regard to the time scales of the current-voltage and carrier density-photon density system, the current-voltage time scale is given by the RC value. When the LD is lasing, the E and N time scales are much faster than the RC time scale and therefore the laser typically follows the current modulation. However, there may be instances where the laser output is faster than the current modulation, as shown in section 5. This occurs because the modulation is switching the gain of the laser which has a faster dynamics than the modulated current pulse.

Optical Materials EXPRESS

3. Nanoscale resonant tunneling diode spike pulse generator

3.1. Self-oscillations and slow-fast dynamics

In this section, Eqs. (1), (2) with $V_m(t) = V_0$ are considered. This corresponds to the nanoRTD biased with a constant input voltage. It is well known from the literature that micro and nanoscale RTDs exhibit self-oscillations (i.e., limit cycle) in both current and voltage when biased in the NDC region and respond with a constant, DC output (i.e., fixed point of equilibrium) when biased in either PDC region [28,34–37]. Numerical simulations show that, the specific range of input bias voltage for which the RTD presented here exhibits self-oscillations lies in between $V_0 = 613$ mV and $V_0 = 722.9$ mV (see Fig. 2). These values are very close to the peak and valley of the I-V characteristic (see section 2). Far from the bifurcation points, the amplitude and period of the self oscillations have little dependence on V_0 (about 290 mV and 330 ps, respectively). This is the consequence of a phenomenon known as *slow-fast dynamics* [36,37]. Given the small coefficient C/L, the change rate of V in Eq. (1) is negligible and the orbit $(V(t), I(t))$ remains close to the I-V characteristic in the PDC regions, until it reaches either the peak or the valley, where it quickly jumps towards the other PDC region. Consequently, the voltage exhibits two slow stages and two fast stages in each period [36]. The quick jumps are perpendicular to the I-direction on the phase plane, and thus the current does not exhibit fast stages. Also, the peak and valley currents of the self-oscillations are very similar to those of the I-V characteristic. Since only the current $I(t)$ is used to pump the LD in Eqs. (3), (4), the optical variables (E, N), do not exhibit fast stages either.

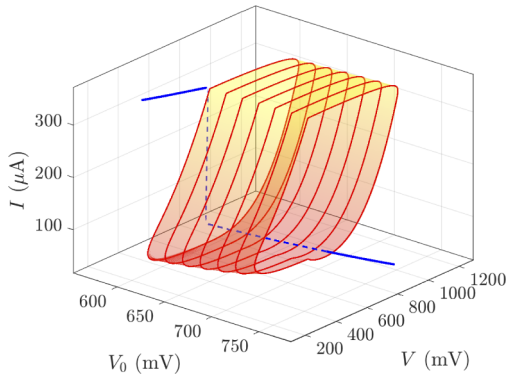

Fig. 2. Equilibrium solutions of Eqs. (1), (2) in terms of V_0, including stable fixed point (solid blue line), unstable fixed point (dashed blue line) and stable limit cycle (solid red lines and gradient colored surface).

From the nonlinear dynamics point of view, the fixed output corresponds to a fixed point branch given by the intersection of the nullclines; the RTD I-V characteristic, $I - f(V) = 0$ and the circuit's load line, $V_0 - V - RI = 0$. On the other hand, the self-oscillations correspond to a limit cycle branch that emerges from the fixed point at two Andronov-Hopf (AH) bifurcations. These bifurcations occur at values of V_0 close to the peak and valley of the I-V curve. The fixed point branch is unstable in between the AH bifurcations and stable elsewhere. As a consequence of the slow-fast dynamics, the limit cycle is a canard solution and its size increases explosively from the AH bifurcations [36,37].

3.2. Excitability

A physical system is referred to as *excitable* if it responds to an external perturbation with a large amplitude trajectory before returning to its natural state of equilibrium, provided that such perturbation is over a certain intensity threshold, regardless of its intensity or nature. On the

Optical Materials EXPRESS

other hand, responses to sub-threshold perturbations are negligible. Because if this, it is said that excitable systems exhibit *all-or-none* responses [19]. The duration of the response to a supra-threshold perturbation is referred to as refractory time or lethargic time. During this time, the excitable system is unable to respond to a second perturbation, regardless of its intensity. The notion of excitability was first coined in the field of neuroscience but it is pertinent in other fields as diverse as neuron-like semiconductors [38], signal generation [39–41] and image processing [42].

The RTD circuit described by Eqs. (1), (2) is, indeed, excitable. When the circuit is biased at $V_0 = 750$ mV (i.e., in the second PDC region but close to the NDC region), it remains steady at about $I = 74$ μA. In the context of numerical simulations, the system can be perturbed by displacing the current from its stable equilibrium, i.e., by giving an arbitrary initial condition. In Fig. 3, simulations of Eqs. (1), (2) are run with different initial conditions along the circuit's load line, with initial currents ranging from 70 μA down to 50 μA. If the initial current is over 60 μA (i.e., close to the steady current), the current quickly returns to its steady value after some relaxation oscillations. However, if the initial current is under 60 μA (i.e., beyond the threshold), the circuit responds with a large current spike, before returning to its rest value, preceded by relaxation oscillations as well. This current spike is reminiscent to a single self-oscillation. The system also exhibits excitable current spikes when the circuit is biased in the first PDC region, close to the NDC region. In an actual experiment, the circuit can be perturbed by injecting a brief voltage or current pulse, shorter than the refractory time.

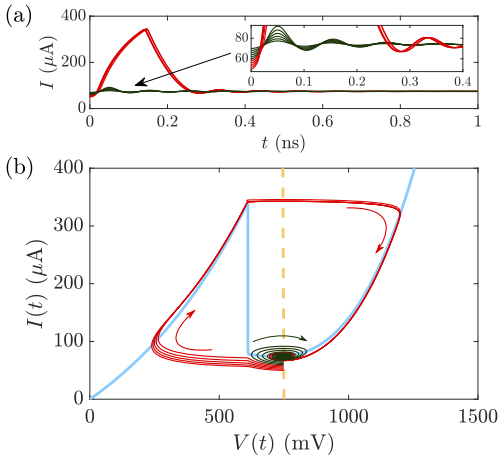

Fig. 3. Simulations of Eqs. (1), (2) with the RTD biased at $V_0 = 750$ mV. Initial conditions lay on the load line, with initial currents ranging from 50 to 70 μA. *a*) Current profiles over time. The inset zooms over the responses to sub-threshold initial currents. *b*) Current-voltage trajectories on the phase plane. Responses to supra-threshold (sub-threshold) initial currents are plotted in red (green).

4. Nanolaser diode

In this section, the response of the nanoLD driven by a DC current source is studied. Semiconductor lasers are responsive in proportion to an input current provided that such current is over a certain threshold. The standard rate equations reproduce this response as a transcritical bifurcation [43]. When no external modulation and no noise are considered in Eqs. (3), (4) (i.e., $I = 0$,

Optical Materials EXPRESS

$\xi_x(t) = \xi_y(t) = 0$), the stable steady state is a piecewise function of the input bias current,

$$S = \max\left(0, \tau_p\left(\frac{J}{q_e} - (\gamma_l + \gamma_m + \gamma_{nr})\left(N_0 + \frac{1}{\gamma_m \tau_p}\right)\right)\right), \tag{6}$$

$$N = \min\left(\frac{J}{(\gamma_l + \gamma_m + \gamma_{nr})q_e}, N_0 + \frac{1}{\gamma_m \tau_p}\right), \tag{7}$$

Therefore, the threshold current is found to be,

$$J_{tr} = q_e\,(\gamma_l + \gamma_m + \gamma_{nr})\left(N_0 + \frac{1}{\gamma_m \tau_p}\right) = 337.54\,\mu\text{A}. \tag{8}$$

The noise, however, has the universal property of turning bifurcations into smooth transitions [44]. This effect can be appreciated by computing the mean value of S and N from numerical simulations of Eqs. (3), (4). The results are illustrated in Fig. 4. For J under the threshold J_{tr}, $\langle S\rangle$ is negligible, while $\langle N\rangle$ is linearly proportional to J. As J crosses the threshold, $\langle S\rangle$ steadily begins to increase at a linear rate while $\langle N\rangle$ saturates. The standard deviations are shown as error bars in Fig. 4. S has a small deviation (less than 10) for $J<J_{tr}$ but as the threshold current is crossed, the deviation increases and saturates at about 800. On the other hand, the standard deviation of N remains small in relation to its average (order 1%).

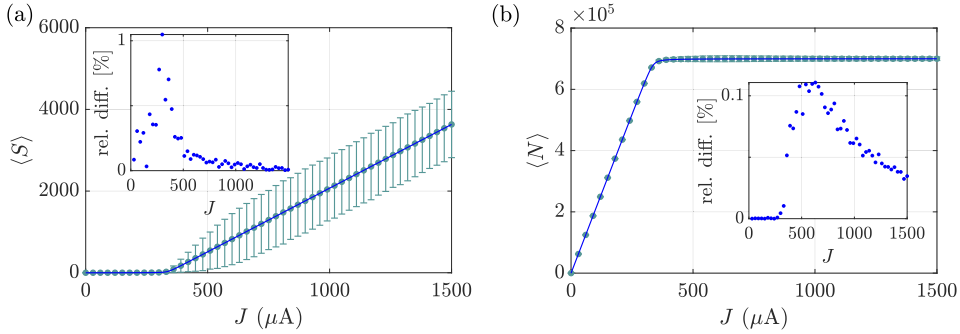

Fig. 4. Mean values of the photon number (a) and carrier number (b) estimated from numerical simulations of stochastic Eqs. (3,4) with $I = 0$ (cyan dots with error bars accounting for standard deviation) and stable steady states of deterministic Eqs. (10,11) (blue lines) versus input bias current. The insets show the relative difference between stochastic and deterministic estimations.

Here, we propose a deterministic model that describes the expected value of the photon and carrier numbers as well as the smooth transition discussed above. To this end, a stochastic equation accounting for the photon number $S = E\bar{E}$ is derived by using Eq. (3), its conjugate and the differentiation rules from stochastic calculus [45],

$$\frac{dS}{dt} = \left(\gamma_m(N - N_0) - \frac{1}{\tau_p}\right)S + \gamma_m N + \sqrt{\gamma_m N S}\,\xi(t), \tag{9}$$

where $\xi(t)$ is a time-uncorrelated white noise function. The term $\gamma_m N$ arises from the fact that the noise functions in Eq. (3) represent random fluctuations with zero mean value and nonzero variance [45]. By considering Eqs. (4), (9) without any fluctuations nor external modulation, we

Optical Materials EXPRESS

reach out to an enhanced deterministic model,

$$\frac{dS}{dt} = \left(\gamma_m(N - N_0) - \frac{1}{\tau_p}\right) S + \gamma_m N, \tag{10}$$

$$\frac{dN}{dt} = \frac{J}{q_e} - (\gamma_l + \gamma_m + \gamma_{nr})N - \gamma_m(N - N_0)S. \tag{11}$$

The stable steady state solution of Eqs. (10), (11) is found to be,

$$N = \frac{B - \sqrt{B^2 - 4AC}}{2A}, \tag{12}$$

$$S = \tau_p \left(\frac{J}{q_e} - (\gamma_l + \gamma_{nr})N\right), \tag{13}$$

where A, B, C are given by,

$$A = \tau_p \gamma_m (\gamma_l + \gamma_{nr}), \tag{14}$$

$$B = \tau_p \gamma_m \left(\frac{J}{q_e} + (\gamma_l + \gamma_{nr})N_0\right) + (\gamma_l + \gamma_m + \gamma_{nr}) \tag{15}$$

$$C = (1 + \tau_p \gamma_m N_0)\frac{J}{q_e}. \tag{16}$$

The expressions given by Eqs. (12), (13) are plotted in Fig. 4 as functions of J. The curves are similar to those given by Eqs. (6), (7), although the transition along the threshold current J_{tr} is smooth. More importantly, Eqs. (12), (13) provide reasonable analytical estimations for the mean values $\langle S \rangle$ and $\langle N \rangle$ discussed above, with a relative error under 1% for the former and under 0.12% for the latter (see insets).

The eigenvalues associated with the stable steady state are plotted as functions of J in Fig. 5. For J under 300 μA, one of the eigenvalues remains practically constant at about $-3\,\mathrm{ns}^{-1}$ while the other one is also negative with a magnitude in the order of $10^3\,\mathrm{ns}^{-1}$, which decreases linearly with J. At $J = 359\,\mu$A, the eigenvalues become conjugate complex numbers. The real part remains negative with a magnitude in the order of $10^1\,\mathrm{ns}^{-1}$ while the imaginary part increases as a square root. Thus, a second threshold current is set where the steady state transitions from stable node to stable focus. This transition is also present when no noise is considered in the standard rate Eqs. (3), (4). However, the presence of noise has a quantitative effect on it.

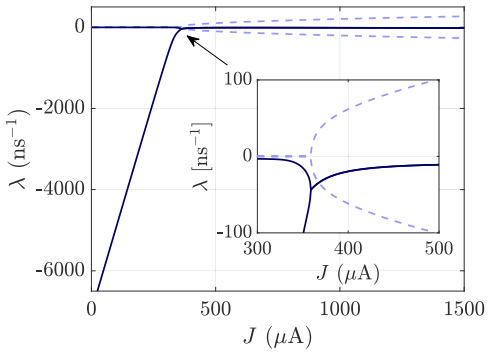

Fig. 5. Real (solid lines) and imaginary (dashed lines) parts of the eigenvalues of the stable steady state of Eqs. (10), (11) versus the input bias current J. The inset zooms over the node-focus transition.

Optical Materials EXPRESS

5. Nanolaser driven by RTD-generated current pulses

In this section, the nanoLD is pumped with excitable current pulses generated by the nanoRTD biased in the proximity to the NDC region and driven with square voltage pulses. Two cases will be considered separately: a nanoRTD biased in the first PDC region modulated with positive pulses, and a nanoRTD biased in the second PDC region modulated with negative pulses.

5.1. RTD biased in the first PDC region

The positive square voltage pulse train $V_m(t)$ driving the RTD has a 600 mV bias, 100 mV amplitude, 2 ns period and 2.5% duty cycle (i.e., 50 ps pulse length). Figure 6(a) zooms over a single period of $V_m(t)$ and shows the excitable current response from the RTD. After a short latency lapse of about 20 ps, the steady state current (328 μA) decreases down to 45 μA and then returns to the steady state after a time roughly estimated in 0.5 ns.

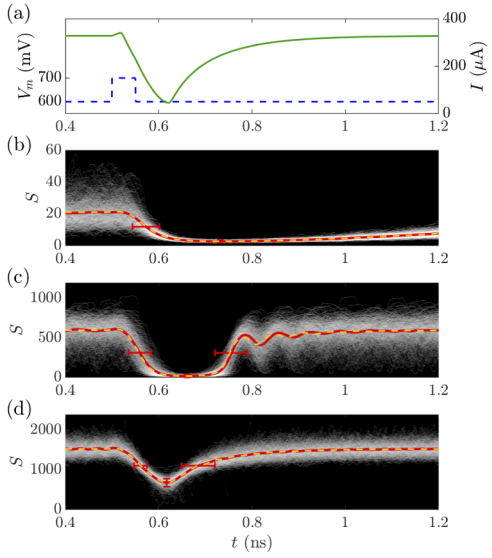

Fig. 6. a) Voltage pulse driving the nanoRTD (blue dashed line) and its excitable response in current (green solid line). b-d) NanoLD optical output for different input bias DC currents, including individual realizations of the stochastic system (white lines), their ensemble average (red solid line), pulse distortion (vertical error bars), time jitter (horizontal error bars) and simulations of the deterministic system (yellow dashed line). All curves have been moving-averaged over a 50 ps window. *b*) $J = 0$ μA, *c*) $J = 200$ μA, *d*) $J = 500$ μA.

To study the response of the LD to the RTD excitable current pulses, 100 realizations of the system of Eqs. (1–4) are run over 5 modulation periods, thus generating a total of 500 responses. Then, these responses are ensemble-averaged. The results are summarized in Fig. 6. The RTD steady state current is higher than the threshold current ($J_{tr} = 337.54$ μA) that turns the LD on, but only slightly so (panel *b*). Therefore, its response is too weak ($S = 21$) and, although the current pulse drives the LD output down to zero, it makes no practical difference. Moreover, the LD takes a much longer time to return to its steady state than the pulse duration. This occurs because when the input current is close to or under J_{tr}, one of the eigenvalues is too small (see Fig. 5), so the relaxation time is too long. When an additional bias current of 200 μA is injected into the LD (panel c), the latter responds with a higher output ($S \approx 550$) except during the pulse, which lowers the current down to 245 μA (sub-threshold) and turns the LD off. After the pulse, the LD returns to its steady state, preceded by relaxation oscillations, since the LD steady state

Optical Materials EXPRESS

has complex eigenvalues, as discussed in section 4. The relaxation oscillations are quite damped and do not affect the transmission of information. The LD turning off in response to the current spike can be interpreted as a single bit of information being transmitted. In that regard, the relaxation oscillations that follow are relatively small relative to the emission rest value and do not turn the LD off again. Finally, When a higher bias current of 500 μA is injected (panel *d*), the LD is permanently emitting, but the pulse momentarily lowers the LD emission intensity, successfully generating a negative light pulse. The relaxation oscillations are still present, but they are small relative to the pulse size.

While the system of Eqs. (1–4) is stochastic in nature, it can be turned into a deterministic system by replacing Eqs. (3), (4) with Eqs. (10), (11). This system provides a description of the expected values of the variables V, I, S, N in real time. In Fig. 6, the deterministic estimation of $\langle S \rangle$ is plotted together with the ensemble average of S from individual realizations of the stochastic system, showing that both curves are in very good agreement regardless of J.

In order to provide a simple description of the nanoLD response (which consists of 500 response pulses), a number of quantities are defined, based on the eye diagram techniques to characterize digital signals [24,25]. In addition to the ensemble average of photon number at rest and at the pulse valley, the *distortion* is given by the standard deviation of the valley values. These three quantities are plotted as functions of J in Fig. 7(a). The photon number rest value seems to increase linearly with J; what is actually happening is that the rest value reproduces the transcritical bifurcation from Fig. 4, displaced to the left in 328 μA, the steady state current from the RTD. On the other hand, the pulse depth remains close to zero for J<200 μA, since S cannot take negative values. As J increases, so does the valley value, at the same rate as the rest value. Consequently, the pulse amplitude saturates at about 200 photons. In regards to the pulse distortion, it increases with J from zero to a peak of 35 photons at J = 420 μA and then another peak of similar height at J = 850 μA.

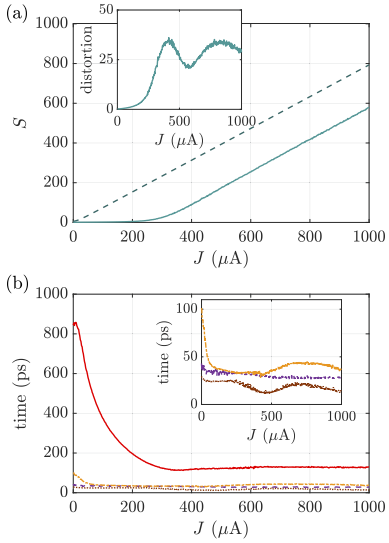

Fig. 7. *a*) NanoLD optical output rest value (dashed cyan line) and pulse valley value (solid cyan line). Inset: distortion at the pulse valley. *b*) Optical pulse FWHM (solid red line), response delay (dashed purple line), before pulse-jitter time (dotted brown line) and after pulse-jitter time (dashed-dotted yellow line). Inset: zooming over the 0-100 ps range.

The pulse width is described in terms of its full-width at half minimum (FWHM), response delay and *jitter* times [24,25]. The response delay is defined as the lapse between the onset of the

Optical Materials EXPRESS

input square voltage pulse and the onset of the LD response, which is in turn defined as the LD pulse reaching 10% of its amplitude. The jitter times are defined as the standard deviations of the time when the pulse reaches 50% of its amplitude before and after the valley (the jitter times are also illustrated in Fig. 6 as horizontal error bars). These quantities are plotted as functions of J in Fig. 7(b). For J<200 μA, the FWHM is quite long (above 200 ps, with a peak value of 800 ps) due to the slow relaxation time. After the peak, the FWHM decreases and above 400 μA, it remains between 110 and 120 ps. Finally, the response delay and jitter times are in the order of the tens of picoseconds, regardless of J.

Summarizing, the RTD-LD biased in the proximity to the I-V curve peak can emit negative optical pulses with sufficiently high power and small distortion and jitter, provided that an additional bias current above 200 μA is injected into the LD. Still this is not an energy-efficient option, as the LD is always or almost always emitting light.

5.2. RTD biased in the second PDC region

The negative square voltage pulse train $V_m(t)$ driving the RTD has a 750 mV bias, 100 mV depth, 2 ns period and 2.5% duty cycle (i.e., 50 ps pulse length). Figure 8(a) shows a single period of $V_m(t)$ together with the RTD excitable response pulse, which reaches a maximum current of 340 μA, with a length of roughly 250 ps. After this pulse, the current returns to its steady state value (74 μA). Note that the excitable response exhibits a short delay time (about 30 ps) since the excitable response is preceded by a slight latency period.

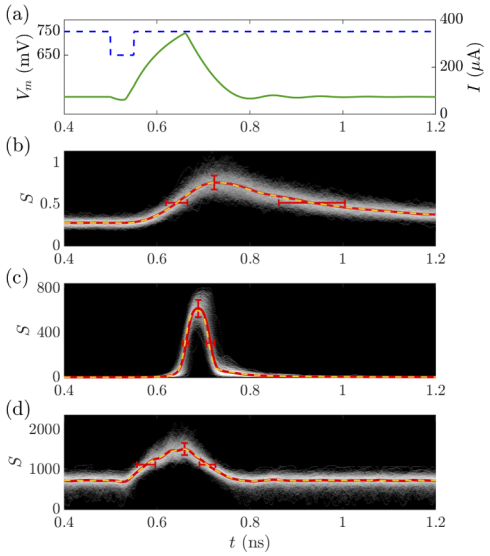

Fig. 8. a) Voltage pulse driving the nanoRTD (blue dashed line) and its excitable response in current (green solid line). b-d) NanoLD optical output for different input bias DC currents, including individual realizations of the stochastic system (white lines), their ensemble average (red solid line), pulse distortion (vertical error bars), time jitter (horizontal error bars) and simulations of the deterministic system (yellow dashed line). All curves have been moving-averaged over a 50 ps window. *b*) J = 0 μA, *c*) J = 214 μA, *d*) J = 500 μA.

Figure 8 summarizes the responses of the nanoLD to the nanoRTD current output and different input bias currents. In each case, 100 realizations of the stochastic system of Eqs. (1–4) are run over 5 modulation periods, thus generating a total of 500 responses. Without an input bias current, the nanoLD response is too weak (panel *b*). Moreover, the response pulse is not even one photon number in height and, since the photon number actually is a discrete variable, the

Optical Materials EXPRESS

nanoLD simply fails to turn on. This occurs because the valley current of the nanoRTD I-V curve is well below the nanoLD threshold current, J_{tr}. Although $I(t)$ surpasses J_{tr}, it does so for a short time and, since the nanoLD relaxation time is too long when J is close to o under J_{tr}, the nanoLD is unable to respond properly to real-time changes in $I(t)$. This phenomenon is known as *critical slowing down* and has been observed in theoretical and experimental problems involving a transcritical bifurcation [46–49]. As the bifurcation is swept over, the system remains in the now unstable zero state, transitioning to the nonzero state when the control parameter is well above the critical point, regardless of its change rate.

An optimal bias current to momentarily turn the nanoLD on and produce a short yet high optical pulse is found to be $J = 214\ \mu$A (panel *c*), with a relatively long response delay (about 150 ps) as the only drawback, consequence of the critical slowing down that is more notorious since the nanoLD is driven way over the threshold. When the current is lowered, there is no critical slowing down [46,47], and the nanoLD turns off faster than it turned on, thus its short duration (roughly 0.5 ns). For a sufficiently high bias current (over 250 μA), the total current $J + I(t)$ is always above J_{tr} and thus the nanoLD is permanently emitting. However, the current pulse from the nanoRTD momentarily increases its power, thus producing an upward optical pulse. This pulse has a much shorter response delay since there is no crossing over the transcritical bifurcation and hence no critical slowing down. More power is consumed in this configuration nonetheless. Finally, Fig. 8 also includes simulations of the deterministic system for all bias currents, showing again that it reproduces the dynamics of the expected optical output in real time quite well.

In analogy to the quantitative characterization from section 5.1, the stochastic response from the nanoLD can be described in terms of the optical output at rest and at the pulse peak. The ensemble averages are shown in Fig. 9(a). As expected, the optical output at rest reproduces the transcritical bifurcation from Fig. 4, displaced to the left in 74 μA, the steady state current from the nanoRTD. As discussed above, for low J (under 200 μA), the nanoRTD fails to turn the nanoLD on, so both the rest and peak values are almost zero. At about 200 μA, the pulse amplitude suddenly increases and saturates roughly at 200 photons. The distortion also increases abruptly and, as J further increases, it continues to grow at a less steep rate, reaching its maximum of about 40 photons roughly at 570 μA.

The pulse width is described in terms of its full-width at half maximum (FWHM), response delay and jitter times. Their plots as functions of J are shown in Fig. 9(b). The FWHM is maximal at $J = 0$ (almost 300 ns) and minimal at $J = 214\ \mu$A (52 ps), in a valley 200 μA wide. In the range of this valley however, the delay time reaches its peak value of 160 ps. Both the response delay peak and the FWHM valley are a consequence of the critical slowing down. As J further increases, the response delay and FWHM saturate at 130 and 40 ps, respectively. For $J>200\ \mu$A, the jitter times before and after the optical pulse peak remain between 9 and 40 ps, and are always much smaller than the FWHM, thus ensuring robustness in the response pulse.

Summarizing, the RTD-LD biased in the proximity to the I-V curve valley can be used to produce a robust response in the form of positive optical pulses, provided that the LD is injected with an additional bias current. There is a narrow range of current for which this pulse is relatively short and light is momentarily emitted. For a higher current, the device is always emitting but the pulse momentarily increases the emission intensity. The latter configuration produces longer pulses and is less power-efficient, but has a shorter response delay.

Optical Materials EXPRESS

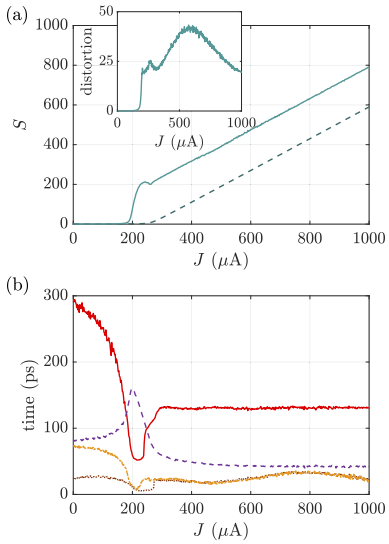

Fig. 9. *a*) NanoLD optical output rest value (dashed cyan line) and pulse peak value (solid cyan line). Inset: distortion at the pulse valley. *b*) Optical pulse FWHM (solid red line), response delay (dashed purple line), before pulse-jitter time (dotted brown line) and after pulse-jitter time (dashed-dotted yellow line).

6. Interconnected master-slave optical neural link

The potential of RTD-LD devices as individual neurons able to generate and propagate pulses at continuous times has been studied extensively [18,26,36,50]. However, integration of such neurons into functional neuromorphic networks is at an early stage of research [51,52]. In this section, two RTD-LD optoelectronic neurons are interconnected, with the second RTD also acting as a photodetector (PD) and therefore, as the connection between the neurons. We assume that this is possible because the RTD layer structure comprises light absorbing layers [18]. The interconnected optical neural link is described by eight equations and variables,

$$C\frac{dV_n}{dt} = I_n - f(V_n) - \delta_{n,2}\kappa|E_1|^2, \tag{17}$$

$$L\frac{dI_n}{dt} = \delta_{n,1}V_m(t) + \delta_{n,2}V_0 - V_n - RI_n. \tag{18}$$

$$\frac{dE_n}{dt} = \frac{1-i\alpha}{2}\left(\gamma_m(N_n - N_0) - \frac{1}{\tau_p}\right)E_n + \sqrt{\tfrac{1}{2}\gamma_m N_n}\left(\xi_n^x(t) + i\xi_n^y(t)\right), \tag{19}$$

$$\frac{dN_n}{dt} = \frac{J_n + I_n}{q_e} - (\gamma_l + \gamma_m + \gamma_{nr})N_n - \gamma_m(N_n - N_0)|E_n|^2, \tag{20}$$

where $n \in \{1, 2\}$ and $\delta_{n,i}$ is the Kronecker symbol. $n = 1$ accounts for the first RTD-LD neuron, labeled as "master" and driven by input square voltage pulses, $V_m(t)$. Its output is injected into the following PD-RTD-LD neuron ($n = 2$), labeled as "slave". V_0 is the slave nanoRTD input bias voltage. The parameters $R, C, L, \alpha, \tau_p, N_0, q_e, \gamma_m, \gamma_l, \gamma_{nr}$ are identical to those of the single RTD-LD covered in section 4. κ is the optical-electrical conversion factor ("responsivity" of the RTD-PD, given by current per number of photons), which receives the optical output from the master nanoLD and converts it into an electrical signal. This signal adds then to the static current of the slave RTD-PD. Figure 10 depicts a simplified scheme of the master-slave neural link.

Optical Materials EXPRESS

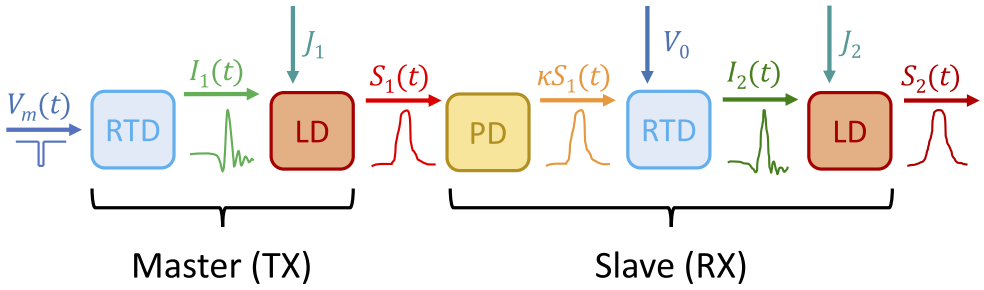

Fig. 10. Schematics of the pulse propagation in the integrated two-neuron circuit.

The configuration of the master RTD-LD neuron is fixed as in section 5.2; the master nanoRTD is biased at the second PDC region and modulated with negative square voltage pulses, and the master nanoLD input bias current is fixed at $J_1 = 214\ \mu$A. Consequently, the master RTD-LD emits short pulses of light as shown in Fig. 11(a) (see see also Fig. 8(c)). By tuning V_0, κ and J_2 properly, the slave PD-RTD-LD can propagate these pulses. Two cases were considered; $V_0 = 600$ mV (i.e., slave RTD biased in the first PDC region) and $V_0 = 750$ mV (i.e., slave RTD biased in the second PDC region). In each case, J_2 was tuned between 0 and 1000 μA.

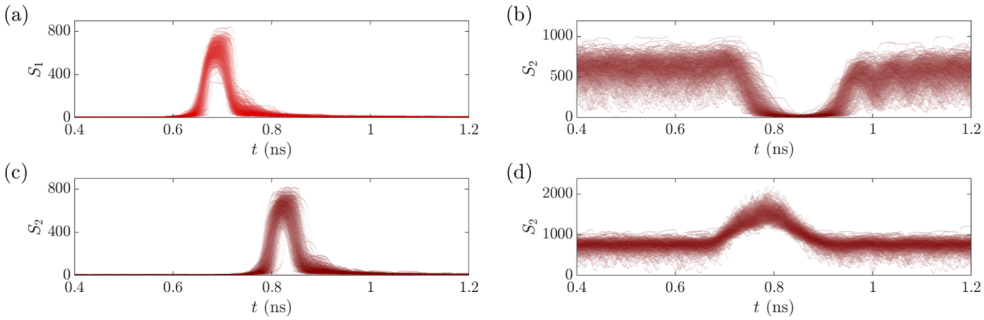

Fig. 11. *a*) Optical output from the master RTD-LD biased at the second PDC region, driven with negative square voltage pulses and tuned at $J_1 = 214\ \mu$A. *b,c,d*) responses from the slave RTD-LD for different values of V_0, κ and J_2: *b*) $V_0 = 600$ mV, $\kappa = 0.11\ \mu$A, $J_2 = 200\ \mu$A. *c*) $V_0 = 750$ mV, $\kappa = 0.05\ \mu$A, $J_2 = 214\ \mu$A. *d*) $V_0 = 750$ mV, $\kappa = 0.05\ \mu$A, $J_2 = 500\ \mu$A.

It is important to emphasize here that a supra-threshold positive light pulse is able to elicit an excitable response from the slave RTD (and thus from the slave LD) regardless of its bias (unlike the voltage pulse, which has to be negative if the RTD is biased close to the valley). This is because the perturbations are different in nature. The voltage pulse is present in the second RTD equation (i.e., Eq. (1) and Eq. (17)) and displaces the load line horizontally, while the optical pulse appears in the first RTD equation (i.e., Eq. (2) and Eq. (18)) and displaces the I-V characteristic vertically.

Since the pulse injected into the slave nanoRTD is stochastic in nature, so is its current output. In that sense, the PD conversion coefficient κ needs to be chosen properly to generate a single pulse to each pulse injected. If κ is too small, so are the pulses injected into the slave nanoRTD and some (or all of them) fail to trigger the excitable response. On the other hand, if κ is too large, the fluctuations in the current injected into the slave nanoRTD are also enlarged, and they may trigger the excitable response at moments when no pulse is being injected. An optimal choice for κ is found to be 0.11 μA when $V_0 = 600$ mV and 0.05 μA when $V_0 = 750$ mV.

Optical Materials EXPRESS

Responses of the slave PD-RTD-LD under different configurations are shown in Fig. 11. The slave neuron responds with negative optical pulses when biased at the first PDC region (panel Fig. 11(b)), and with positive optical pulses when biased at the second PDC region (panels Fig. 11(c) and 11(d)), just like the single RTD-LD. Moreover, the slave PD-RTD-LD bias voltage and bias current chosen in Fig. 11(b), 11(c), and 11(d) are the same as those of the single RTD-LD chosen in Fig. 6(c), Fig. 8(c) and Fig. 8(d), respectively. In consequence, the responses are almost identical in each case, given the all-or-none character of the RTD excitable response. The only remarkable difference is the response delay, which is significantly increased in comparison with the single RTD-LD. This happens because the pulse propagation along the two-neuron neural link involves more steps and thus, there are more accumulated delays adding up. When the slave RTD-LD optical response is characterized in terms of pulse amplitude, width, distortion and jitter times, their curves as function of J_2 are almost identical to those portrayed in Fig. 7 and Fig. 9. The only exception is, as mentioned above, the increased response delay, as shown in Fig. 12. The increment is in about 195 ps when the RTD (slave RTD in the case of the integrated circuit) is biased in the first PDC region and about 135 ps when the RTD is biased in the second PDC region. This difference is attributed to the difference in response delay between the RTD responses for each bias. It can be seen in Fig. 11 that the RTD takes a longer time to initiate the excitable response when it is biased in the first PDC region.

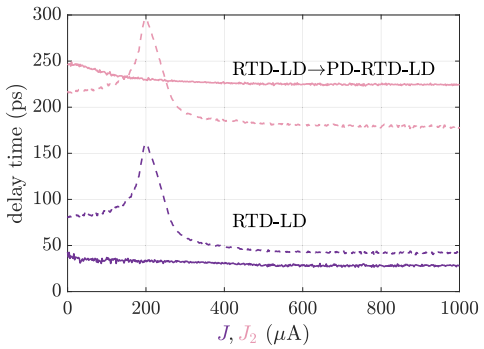

Fig. 12. Response delay of a single RTD-LD neuron versus J (purple lines) and that of an integrated two-neuron circuit versus J_2 (pink lines), with the (slave) RTD biased in the first PDC region (solid lines) and the second PDC region (dashed lines).

7. Conclusions

In this paper, a nanopillar metal-cavity consisting of a resonant tunneling diode (RTD) integrated with a nanolaser diode (LD), has been demonstrated as an excitable optical pulse generator. This optoelectronic device emulates the behavior of biological neurons and therefore has a potential application as individual blocks in neuromorphic processors, with aims to execute spiking neural network algorithms efficiently in terms of time and energy consumption. The RTD-LD neuron can be set to emit light permanently, and a pulse is produced by a momentary increase, decrease or deactivation in the emission. In a more power-efficient configuration, the neuron emits pulses under a no-emission rest state. In all cases, the optical response is quantitatively characterized by resorting to eye diagram methods and measuring the emission rest value, pulse amplitude, FWHM and response delay. The fluctuating nature of the response is also quantified in terms of the amplitude distortion and jitter times. By choosing the system parameters properly, the FWHM (and thus, energy per spike) is minimized, as well as the jitter (which ensures a robust response), but the delay response is maximized, reaching values of 50, 9 and 150 ps, respectively. In particular, the FWHM provides a good notion of both the excitable pulse length and the

Optical Materials EXPRESS

refractory time of the neuron's response. However, a precise calculation of the refractory time requires a different study, where two consecutive short, supra-threshold square voltage pulses are injected into the neuron in order to find out the shortest time separation between said pulses for which the neuron fires two distinct light pulses. Such study would involve a significant effort and numerous simulations, given the parameters involved, types of excitable pulses and the noise in the neuron.

Transmission of information between two optoelectronic neurons connected via a photodetector is also demonstrated. In particular, the 50 ps short pulse is successfully propagated. The additional input bias current injected into the LD allows to obtain the different types of pulses covered in this work. However, this is not a practical choice in actual experiments and designs. By adjusting the RTD epi-layers it is possible to get the peak and valley current values that fit the requirements for the optimization of the performance of the RTD-LD nodes, thus avoiding the need of extra-current sources.

Pulse propagation through a longer sequence of optoelectronic neurons is yet to be studied, with aims to predicting the performance of spiking neural neural networks made of these neurons. Given the all-or-none character of the RTD excitable response, the pulse is regenerated after each RTD-LD node. It is worth noting that as a consequence of the stochastic character of the nanoLD, the time when a given downstream neuron in the network fires a pulse is expected to exhibit slight variations when studied over multiple simulations (or experiments). Indeed, an approach towards a similar problem has already been carried out by Romeira et al., where a single autaptic electronic neuron connected to itself via a delay line is considered [50]. Such a system is modeled with a delayed differential equation but it is ultimately equivalent to an array of multiple neurons connected in sequence. The pulse propagation is shown to be equivalent to the random motion of a spatiotemporal localized structure in a finite, periodic, one-dimensional layer, subjected to drift and Brownian motion, as a consequence of the inherent response delay and noise, respectively.

Funding. H2020 Future and Emerging Technologies (828841); UK Research and Innovation Turing AI Acceleration Fellowships Programme (EP/V025198/1).

Acknowledgments. The authors are supported by the European Commission through the H2020-FET-OPEN Project "ChipAI". The authors also acknowledge Víctor Dolores-Calzadilla and Ekaterina Malysheva from the Eindhoven University of Technology for their fruitful contributions on nanolasers. The team at the University of Strathclyde acknowledges support from the UKRI Turing AI Acceleration Fellowships Programme.

Disclosures. The authors declare no conflicts of interest.

Data availability. Data underlying the results presented in this paper are not publicly available at this time but may be obtained from the authors upon reasonable request.

References

1. J. Von Neumann, "First draft of a report on the EDVAC," (1945). Unpublished.
2. P. A. Merolla, J. V. Arthur, R. Alvarez-Icaza, A. S. Cassidy, J. Sawada, F. Akopyan, B. L. Jackson, N. Imam, C. Guo, Y. Nakamura, B. Brezzo, I. Vo, S. K. Esser, R. Appuswamy, B. Taba, A. Amir, M. D. Flickner, W. P. Risk, R. Manohar, and D. S. Modha, "A million spiking-neuron integrated circuit with a scalable communication network and interface," Science **345**(6197), 668–673 (2014).
3. "Intel advances neuromorphic with Loihi 2, new lava software framework and new partners," (2021). Https://www.intel.com/content/www/us/en/newsroom/news/intel-unveils-neuromorphic-loihi-2-lava-software.html.
4. "The BRAIN Initiative," Https://braininitiative.nih.gov/.
5. S. Ward-Foxton, "Innatera unveils neuromorphic AI chip to accelerate spiking networks," (2021). Https://www.eetimes.com/innatera-unveils-neuromorphic-ai-chip-to-accelerate-spiking-networks.
6. D. A. B. Miller, "Attojoule optoelectronics for low-energy information processing and communications," J. Lightwave Technol. **35**(3), 346–396 (2017).
7. B. J. Shastri, M. A. Nahmias, A. N. Tait, A. W. Rodriguez, B. Wu, and P. R. Prucnal, "Spike processing with a graphene excitable laser," Sci. Rep. **6**(1), 19126 (2016).
8. B. Romeira, R. Avó, J. M. L. Figueiredo, S. Barland, and J. Javaloyes, "Regenerative memory in time-delayed neuromorphic photonic resonators," Sci. Rep. **6**(1), 19510 (2016).

Optical Materials EXPRESS

9. J. Feldmann, N. Youngblood, C. D. Wright, H. Bhaskaran, and W. H. P. Pernice, "All-optical spiking neurosynaptic networks with self-learning capabilities," Nature **569**(7755), 208–214 (2019).
10. T. Deng, J. Robertson, Z.-M. Wu, G.-Q. Xia, X.-D. Lin, X. Tang, Z.-J. Wang, and A. Hurtado, "Stable propagation of inhibited spiking dynamics in vertical-cavity surface-emitting lasers for neuromorphic photonic networks," IEEE Access **6**, 67951–67958 (2018).
11. M. A. Nahmias, B. J. Shastri, A. N. Tait, and P. R. Prucnal, "A leaky integrate-and-fire laser neuron for ultrafast cognitive computing," IEEE J. Sel. Top. Quantum Electron. **19**(5), 1–12 (2013).
12. M. Hejda, J. Robertson, J. Bueno, J. A. Alanis, and A. Hurtado, "Neuromorphic encoding of image pixel data into rate-coded optical spike trains with a photonic VCSEL-neuron," APL Photonics **6**(6), 060802 (2021).
13. B. Ellis, M. A. Mayer, G. Shambat, T. Sarmiento, J. Harris, E. E. Haller, and J. Vučković, "Ultralow-threshold electrically pumped quantum-dot photonic-crystal nanocavity laser," Nat. Photonics **5**(5), 297–300 (2011).
14. K. Takeda, T. Sato, A. Shinya, K. Nozaki, W. Kobayashi, H. Taniyama, M. Notomi, K. Hasebe, T. Kakitsuka, and S. Matsuo, "Few-fj/bit data transmissions using directly modulated lambda-scale embedded active region photonic-crystal lasers," Nat. Photonics **7**(7), 569–575 (2013).
15. G. Crosnier, D. Sanchez, S. Bouchoule, P. Monnier, G. Beaudoin, I. Sagnes, R. Raj, and F. Raineri, "Hybrid indium phosphide-on-silicon nanolaser diode," Nat. Photonics **11**(5), 297–300 (2017).
16. M. T. Hill, Y.-S. Oei, B. Smalbrugge, Y. Zhu, T. de Vries, P. J. van Veldhoven, F. W. M. van Otten, T. J. Eijkemans, J. P. Turkiewicz, H. de Waardt, E. J. Geluk, S.-H. Kwon, Y.-H. Lee, R. Nötzel, and M. K. Smit, "Lasing in metallic-coated nanocavities," Nat. Photonics **1**(10), 589–594 (2007).
17. R. F. Oulton, V. J. Sorger, T. Zentgraf, R.-M. Ma, C. Gladden, L. Dai, G. Bartal, and X. Zhang, "Plasmon lasers at deep subwavelength scale," Nature **461**(7264), 629–632 (2009).
18. B. Romeira, J. Figueiredo, and J. Javaloyes, "Nanoleds for energy-efficient and gigahertz-speed spike-based sub-λ neuromorphic nanophotonic computing," Nanophotonics **9**(13), 4149–4162 (2020).
19. E. M. Izhikevich, *Dynamical Systems in Neuroscience: The Geometry of Excitability and Bursting*, Computational neuroscience (MIT Press, 2007).
20. Y. Zhang, J. Robertson, S. Xiang, M. Hejda, J. Bueno, and A. Hurtado, "All-optical neuromorphic binary convolution with a spiking vcsel neuron for image gradient magnitudes," Photonics Res. **9**(5), B201–B209 (2021).
21. Y. Zhang, S. Xiang, X. Cao, S. Zhao, X. Guo, A. Wen, and Y. Hao, "Experimental demonstration of pyramidal neuron-like dynamics dominated by dendritic action potentials based on a vcsel for all-optical xor classification task," Photonics Res. **9**(6), 1055–1061 (2021).
22. B. J. Shastri, A. N. Tait, T. Ferreira de Lima, W. H. P. Pernice, H. Bhaskaran, C. D. Wright, and P. R. Prucnal, "Photonics for artificial intelligence and neuromorphic computing," Nat. Photonics **15**(2), 102–114 (2021).
23. B. Romeira and A. Fiore, "Purcell effect in the stimulated and spontaneous emission rates of nanoscale semiconductor lasers," IEEE J. Quantum Electron. **54**(2), 1–12 (2018).
24. A. Company, "Application Note no. 11410-00533 - Understanding Eye Pattern Measurements," (2010).
25. O. S. Company, "Application Note AND9075/D - Understanding Data Eye Diagram Methodology for Analyzing High Speed Digital Signals," (2015).
26. B. Romeira, J. Javaloyes, C. N. Ironside, J. M. L. Figueiredo, S. Balle, and O. Piro, "Excitability and optical pulse generation in semiconductor lasers driven by resonant tunneling diode photo-detectors," Opt. Express **21**(18), 20931–20940 (2013).
27. T. J. Slight, B. Romeira, L. Wang, J. M. L. Figueiredo, E. Wasige, and C. N. Ironside, "A liénard oscillator resonant tunnelling diode-laser diode hybrid integrated circuit: Model and experiment," IEEE J. Quantum Electron. **44**(12), 1158–1163 (2008).
28. J. Wang, A. Al-Khalidi, L. Wang, R. Morariu, A. Ofiare, and E. Wasige, "15-gb/s 50-cm wireless link using a high-power compact iii-v 84-ghz transmitter," IEEE Trans. Microwave Theory Tech. **66**, 4698–4705 (2018).
29. J. N. Schulman, H. J. De Los Santos, and D. H. Chow, "Physics-based RTD current-voltage equation," IEEE Electron Device Lett. **17**(5), 220–222 (1996).
30. H. Yokoyama and S. D. Brorson, "Rate equation analysis of microcavity lasers," J. Appl. Phys. **66**(10), 4801–4805 (1989).
31. J. Mørk and G. L. Lippi, "Rate equation description of quantum noise in nanolasers with few emitters," Appl. Phys. Lett. **112**(14), 141103 (2018).
32. G. Bjork and Y. Yamamoto, "Analysis of semiconductor microcavity lasers using rate equations," IEEE J. Quantum Electron. **27**(11), 2386–2396 (1991).
33. P. R. Rice and H. J. Carmichael, "Photon statistics of a cavity-QED laser: A comment on the laser–phase-transition analogy," Phys. Rev. A **50**(5), 4318–4329 (1994).
34. S. Diebold, K. Nishio, Y. Nishida, J. Kim, K. Tsuruda, T. Mukai, M. Fujita, and T. Nagatsuma, "High-speed error-free wireless data transmission using a terahertz resonant tunnelling diode transmitter and receiver," Electron. Lett. **52**(24), 1999–2001 (2016).
35. R. Izumi, S. Suzuki, and M. Asada, "1.98 thz resonant-tunneling-diode oscillator with reduced conduction loss by thick antenna electrode," in *2017 42nd International Conference on Infrared, Millimeter, and Terahertz Waves (IRMMW-THz)*, (IEEE, 2017), pp. 1–2.
36. I. Ortega-Piwonka, O. Piro, B. Romeira, and J. Javaloyes, "Bursting and excitability in neuromorphic resonant tunneling diodes," Phys. Rev. Appl. **15**(3), 034017 (2021).

Optical Materials EXPRESS

37. I. Ortega-Piwonka, A. E. Teruel, R. Prohens, C. Vich, and J. Javaloyes, "Simplified description of dynamics in neuromorphic resonant tunneling diodes," Chaos **31**(11), 113128 (2021).
38. A. Samardak, A. Nogaret, N. Janson, A. Balanov, I. Farrer, and D. Ritchie, "Spiking computation and stochastic amplification in a neuron-like semiconductor microstructure," J. Appl. Phys. **109**(10), 102408 (2011).
39. D. Goulding, S. P. Hegarty, O. Rasskazov, S. Melnik, M. Hartnett, G. Greene, J. G. McInerney, D. Rachinskii, and G. Huyet, "Excitability in a quantum dot semiconductor laser with optical injection," Phys. Rev. Lett. **98**(15), 153903 (2007).
40. F. Selmi, R. Braive, G. Beaudoin, I. Sagnes, R. Kuszelewicz, and S. Barbay, "Relative refractory period in an excitable semiconductor laser," Phys. Rev. Lett. **112**(18), 183902 (2014).
41. S. Barbay, R. Kuszelewicz, and A. M. Yacomotti, "Excitability in a semiconductor laser with saturable absorber," Opt. Lett. **36**(23), 4476–4478 (2011).
42. L. Kuhnert, K. I. Agladze, and V. I. Krinsky, "Image processing using light-sensitive chemical waves," Nature **337**(6204), 244–247 (1989).
43. S. H. Strogatz, *Nonlinear Dynamics and Chaos (with applications to Physics, Biology, Chemistry and Engineering*) (CRC Press, 2015).
44. G. Agez, M. G. Clerc, and E. Louvergneaux, "Universal shape law of stochastic supercritical bifurcations: Theory and experiments," Phys. Rev. E **77**(2), 026218 (2008).
45. C. W. Gardiner, *Handbook of Stochastic Methods* 2nd Ed. (Springer-Verlag, 1995).
46. J. R. Tredicce, G. L. Lippi, P. Mandel, B. Charasse, A. Chevalier, and B. Picqué, "Critical slowing down at a bifurcation," Am. J. Phys. **72**(6), 799–809 (2004).
47. M. Marconi, C. Métayer, A. Acquaviva, J. M. Boyer, A. Gomel, T. Quiniou, C. Masoller, M. Giudici, and J. R. Tredicce, "Testing critical slowing down as a bifurcation indicator in a low-dissipation dynamical system," Phys. Rev. Lett. **125**(13), 134102 (2020).
48. W. Scharpf, M. Squicciarini, D. Bromley, C. Green, J. Tredicce, and L. Narducci, "Experimental observation of a delayed bifurcation at the threshold of an argon laser," Opt. Commun. **63**(5), 344–348 (1987).
49. P. Mandel and T. Erneux, "Laser lorenz equations with a time-dependent parameter," Phys. Rev. Lett. **53**(19), 1818–1820 (1984).
50. B. Romeira, J. M. L. Figueiredo, and J. Javaloyes, "Delay dynamics of neuromorphic optoelectronic nanoscale resonators: Perspectives and applications," Chaos **27**(11), 114323 (2017).
51. J. Robertson, M. Hejda, J. Bueno, and A. Hurtado, "Ultrafast optical integration and pattern classification for neuromorphic photonics based on spiking VCSEL neurons," Sci. Rep. **10**(1), 6098 (2020).
52. B. Romeira, J. Javaloyes, J. M. L. Figueiredo, C. N. Ironside, H. I. Cantu, and A. E. Kelly, "Delayed feedback dynamics of Liénard-type resonant tunneling-photo-detector optoelectronic oscillators," IEEE J. Quantum Electron. **49**(1), 31–42 (2013).